Progress In Electromagnetics Research M, Vol. 96, 139–146, 2020

Analysis of the Noise Components for Affecting the Imaging Performance of the Synthetic Aperture Interferometric Radiometer (SAIR)

Jinguo Wang*, Zhaozhao Gao, Jie Gu, Shiwen Li, Xiaoyun Zhang, Zitong Dong, Zilong Zhao, Fan Jiang, Bo Qi, and Wei Zhao

Abstract—Microwave radiometer is a high-sensitivity "camera", which realizes high-resolution imaging by receiving the natural radiation signal in microwave band from the observation scene. Due to the imperfection of the system hardware, the measured data include not only the radiated signal of interest but also the noise generated by the system hardware itself. These unexpected noises will affect the imaging performance of the system, especially for the synthetic aperture interferometric radiometer (SAIR). In this paper, the noise behavior of the SAIR system is analyzed and modeled for the first time. Based on the noise behavior model, a method is proposed to pick the optimal averaging time for imaging with high fidelity in the SAIR system. Some experiments are carried out to verify the correctness of the noise behavior model and the optimal averaging time picking method for SAIR. With the noise behavior model and the optimal averaging time picking method, it can provide an effective guide for the SAIR system design, error correction, and reconstruction.

1. INTRODUCTION

Anything above absolute zero radiates energy outward in the form of electromagnetic waves. The microwave radiometric realizes high resolution imaging by receiving the thermal radiation signal generated by the observed scene itself [1]. Since it does not actively transmit signals, the microwave radiometric is widely used in various domains such as security check and remote sensing [2–9].

Due to the non-ideality of the system devices, the measured data contain not only the thermal radiation signal of the observation scene, but also the thermal noise produced by the system hardware itself. These noise components will seriously affect the imaging reconstruction of the microwave radiometric system, especially for the synthetic aperture interference radiometric (SAIR) system [7, 8]. Therefore, it is necessary to analyze the noise components in the microwave radiometric system and reduce the impact of these noises on the imaging performance of the microwave radiometric system.

At present, the noise behavior of the microwave radiometric has been discussed for the total power radiometer. Land et al. modeled and analyzed the noise behavior of the total power radiometer, and utilized the Allen deviation to distinguish different noise components [10]. Different to the total power radiometer, the SAIR realizes the imaging by using the cross-correlation processing between multiple receiving channels [6–8]. Fig. 1 shows the schematic of the SAIR system. Compared with the total power radiometer, the SAIR has more receiving elements and higher system complexity. So, the noise behavior of the SAIR system is more complex than that of the total power radiometer. To our knowledge, there are few reports on the noise behavior analysis of the SAIR system. The main contribution of this paper is to

Received 8 April 2020, Accepted 8 September 2020, Scheduled 22 September 2020

* Corresponding author: Jinguo Wang (wangjinguo09@126.com).

The authors are with the Science and Technology on Electronic Information Control Laboratory, the 29th Research Institute of China Electronics Technology Group Corporation, Chengdu, Sichuan, China.

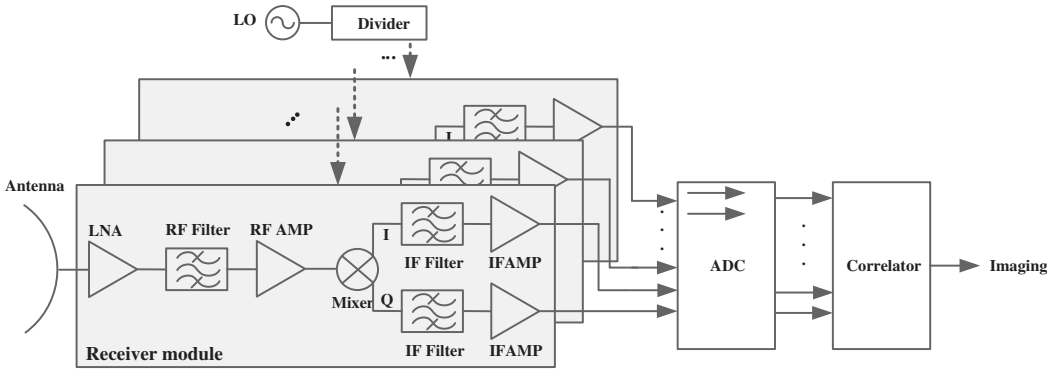

Figure 1. Schematic of the SAIR system.

research the noise behavior of the SAIR system and propose a method for picking the optimal averaging time for imaging in the SAIR system. With the noise behavior model and the optimal averaging time picking method developed in this paper, it provides guidance for the SAIR system design, noise error correction and imaging reconstruction in practical application.

This paper is organized as follows. In Section 2, the noise behavior in SAIR system is analyzed and modeled. Based on the noise behavior model, the method is presented to pick the optimal averaging time of the SAIR system for imaging. In Section 3, the experiments are carried out to validate the accuracy of the presented model and the method. Conclusions are drawn in Section 4.

2. THEORY

2.1. Noise Behavior Model in SAIR System

Based on the principle of the interferometry, the SAIR system measures the data (namely visibility samples) by using the cross-correlation between multiple receiving channels and then recovers the image of the observation scene with the measured visibility samples [1, 2, 11, 12].

Since the basic unit of the SAIR system is a binary interferometer, the measurement diagram of a two-channel binary interferometer is presented in Fig. 2 to model the noise behavior of the SAIR.

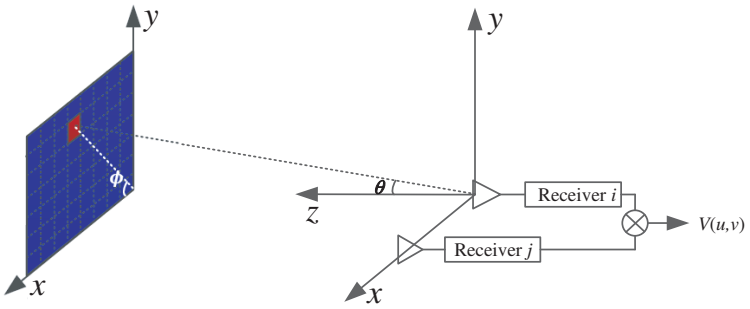

Figure 2. Interference measurement schematic.

As shown in Fig. 1, the RF receiver of the SAIR system consists of the microwave amplifiers, filters, mixers, etc. According to the researches in [10, 16], the Gaussian thermal noise is generated in all the component parts of the microwave amplification and detection circuits. Flicker noise is generated in the active amplifying, detecting and temperature sensing components of the radiometer. Random-walk noise is generated usually due to the short-term changes in the temperature of microwave circuit losses and in amplifier gains. The data measured by each receiver includes not only the thermal signals of

interest, but also other noise components such as the Gaussian noise, flicker or $1/f$ noise and random-walk drift [10, 13–15]. These three types of noise components are commonly met in the microwave radiometry measurements [10]. Therefore, the data measured by SAIR is assumed as follows:

$$\begin{aligned} r_i(t) &= n_{si}(t) + n_i(t) + n_{fi}(t) + n_{ri}(t) \\ r_j(t) &= n_{sj}(t) + n_j(t) + n_{fj}(t) + n_{rj}(t) \end{aligned} \tag{1}$$

where $n_{si}(t)$ denotes the thermal signal of interest measured by receiver i, and $n_i(t)$, $n_{fi}(t)$, and $n_{ri}(t)$ are the Gaussian thermal noise, flicker noise, and random-walk noise generated by the microwave amplification and detection circuits of receiver i, respectively.

By performing cross-correlation between two receivers, the measured visibility samples are expressed as follows

$$\begin{aligned} V_{ij} &= \langle r_i(t) r_j^*(t) \rangle \\ &= \langle n_{si}(t) n_{sj}^*(t) \rangle + \langle n_{si}(t) n_j^*(t) \rangle + \langle n_{si}(t) n_{fj}^*(t) \rangle + \langle n_{si}(t) n_{rj}^*(t) \rangle \\ &+ \langle n_i(t) n_{sj}^*(t) \rangle + \langle n_i(t) n_j^*(t) \rangle + \langle n_i(t) n_{fj}^*(t) \rangle + \langle n_i(t) n_{rj}^*(t) \rangle \\ &+ \langle n_{fi}(t) n_{sj}^*(t) \rangle + \langle n_{fi}(t) n_j^*(t) \rangle + \langle n_{fi}(t) n_{fj}^*(t) \rangle + \langle n_{fi}(t) n_{rj}^*(t) \rangle \\ &+ \langle n_{ri}(t) n_{sj}^*(t) \rangle + \langle n_{ri}(t) n_j^*(t) \rangle + \langle n_{ri}(t) n_{fj}^*(t) \rangle + \langle n_{ri}(t) n_{rj}^*(t) \rangle \end{aligned} \tag{2}$$

Since different noise components are uncorrelated, Eq. (2) is simplified as follows:

$$V_{ij} = P_s + P_f + P_r \tag{3}$$

where P_s includes the power of the Gaussian signal of interest and the Gaussian noise generated by the receivers, and P_f and P_{drift} are the power of the flicker noise and random-walk noise, respectively.

With the visibility samples measured by the SAIR system, the image of the interest scene can be reconstructed by using the inverse Fourier transform [1, 2, 11, 12]:

$$T(\xi, \eta) = \int_{-\infty}^{\infty} \int_{-\infty}^{\infty} V(u, v) \cdot e^{j2\pi(u \cdot \xi + v \cdot \eta)} d\xi d\eta. \tag{4}$$

where $(\xi, \eta) = (\sin\theta\cos\phi, \sin\theta\sin\phi)$, $u = (x_i - x_j)/\lambda$, $v = (y_i - y_j)/\lambda$, $T(\xi, \eta)$ is the brightness temperature distribution of the interest scene.

From Eq. (3), the visibility samples measured by the SAIR system includes not only the Gaussian thermal signal radiated by the interest scene but also the flicker noise and random-walk noise. These noise components can affect the imaging performance of the SAIR system, and make it impossible to image in severe cases. Therefore, it is necessary to distinguish the flicker noise and random-walk noise, and reduce the impacts of the noise components on the SAIR system.

The Allen deviation method can identify and provide excellent differentiation between these three types of noise components because the Gaussian thermal noise, flicker noise and random-walk noise have different power spectral densities [10, 16]. So, the Allan deviation method is used to analyze these noise components in the SAIR system. The Allen deviation is defined as follows [10, 16, 17]:

$$\sigma_y^2(\tau) = \sqrt{\frac{\sum_{i=1}^{N-1} (y_{i+1} - y_i)^2}{2(N-1)}} \tag{5}$$

where y_i is a N point measured data with sampling period τ.

According to Eq. (5), the Allen deviation of the measured samples in SAIR is expressed as:

$$\begin{aligned} \sigma_y^2(\tau) &= \sigma_0^2(\tau) + \sigma_{-1}^2(\tau) + \sigma_{-2}^2(\tau) \\ &= \frac{h_0}{2 \cdot \tau} + 2h_{-1} \cdot \ln 2 + h_{-2} \cdot \frac{(2\pi)^2}{6} \cdot \tau \end{aligned} \tag{6}$$

where $\sigma_0^2(\tau)$, $\sigma_{-1}^2(\tau)$, and σ_{-2}^2 are the Allen deviations of Gaussian noise, flicker noise, and random-walk noise, respectively. τ is the sampling period, and h_0, h_{-1}, and h_{-2} represent the power spectral density coefficients of Gaussian noise, flicker noise, and random-walk noise, respectively.

From Eq. (6), the Allen deviations of these three noise components are different. More specific, the Allen deviation of the Gaussian noise decreases with the increase of sampling time, while that of the random-walk noise increases with the increase of sampling time. The Allen deviation of the flicker noise remains constant with the increase the sampling time. So the power spectral coefficients of three noise components can be obtained by combining the Allen deviation method with the curve fitting method according to Eq. (6). With the obtained power spectral coefficients of three noise components, it can distinguish different noise components and determine the optimal averaging time for imaging.

2.2. Optimal Averaging Time for Imaging in SAIR System

Based on the above analysis, a method is developed to measure the optimal averaging time of the SAIR system in this subsection. With the optimal averaging time of the SAIR system, it can provide guidance for system design, error calibration and high quality inversion imaging.

To make it clear, an example is firstly given as follows. Fig. 3 shows the Allen variation curves of Gaussian noise, flicker noise, random-walk noise and its mixed noise. The lines with triangle, circle and inverted triangle symbols denote the Allen variation curves of the Gaussian noise, flicker noise and random-walk noise, respectively. The line with square symbol denotes the Allen variation curve of the mixed noise.

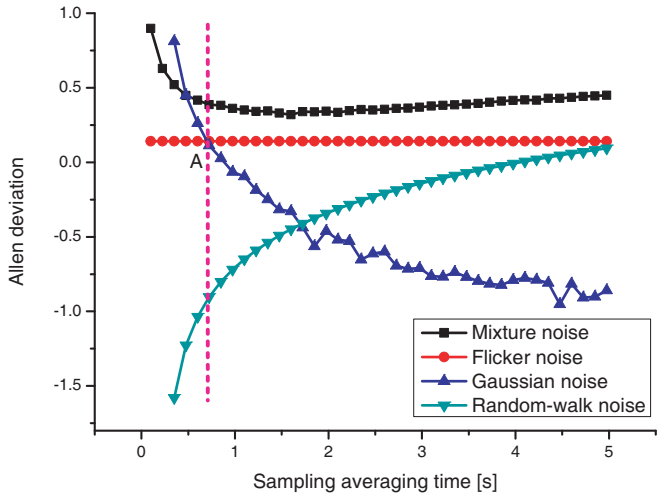

Figure 3. The Allen deviations of Gaussian noise, flicker noise, random-walk noise and its mixed noises.

From Fig. 3, the Gaussian noise predominates below the sampling averaging time A. So, the Allen variance curve of the mixed noise is similar to that of the Gaussian noise. Due to the effect of the flicker noise and random-walk noise, the Allen variance curve of the mixed noise no longer decreases with the increase of sampling time because the flicker noise or random-walk noise predominates above the sampling time A. In other words, the imaging performance or sensitivity of the SAIR system will not be improved even increasing the sampling time. So it is necessary to obtain the optimal sampling averaging time A to ensure the SAIR system with the best imaging performance in practical application.

Rewrite Eq. (6) as:

$$\sigma_y^2(\tau) = \frac{a}{\tau} + b + c \cdot \tau \tag{7}$$

where a, b, and c are related with the power spectral density coefficients of the Gaussian noise, flicker noise and random-walk noise, respectively.

By analyzing the Allen variance of the measured data, the power spectral density coefficients of three noise components can be obtained and then used to calculate the optimal averaging time of SAIR system according to the following equation:

$$\tau_{optimal} = \min\left(\frac{a}{b}, \sqrt{\frac{a}{c}}\right) \tag{8}$$

The processing steps of the proposed method are summarized as follows:

Step 1: For the scene of the extended source (e.g., cold sky), measure the cross-correlation data between different receiving channels of the SAIR system.

Step 2: According to Eq. (5), calculate the Allen variance of the cross-correlation data measured in Step 1.

Step 3: With the Allen variance calculated in Step 2, obtain the power spectral coefficients of the Gaussian noise, flicker noise and random-walk noise by using the curve fitting method according to Eq. (7).

Step 4: Based on the power spectral coefficients of three noise components, calculate the optimal averaging time of SAIR system according to Eq. (8).

It is worth noting that the period of the cross-correlation data measured in Step 1 should be on the order of seconds or more. Besides, the optimal averaging time of SAIR system should be measured multiple times to ensure the accuracy of the measurements.

3. EXPERIMENTAL VALIDATION

In this section, the SAIR system at W band is used to test and verify the effectiveness of the proposed noise behavior model and optimal averaging time picking method. The receiving array of the test system is a staggered y-shaped array with 12 elements, as shown in Fig. 4(a). Fig. 4(b) shows the corresponding *uv* sampling grid coverage in spatial-frequency domain. With the SAIR system, the cold sky scene is observed and the cross-correlation data between different receiving channels in this scene is collected.

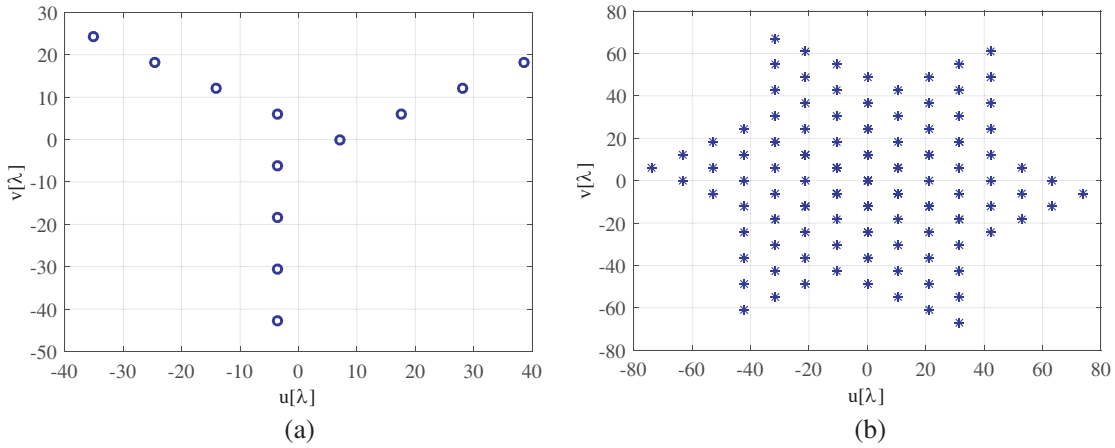

Figure 4. Receiving array of the experimental system: (a) layout of the antenna array; (b) *uv* sampling grid coverage.

The black line in Fig. 5 plots the Allen variance curve of the data measured by channel 1 and channel 2 of the test system. The red line in Fig. 5 plots the corresponding fitting curve. From Fig. 5, the Allen variance of the data received by the test system gradually decreases with the increase of sampling time when the sampling integration time is less than 7 seconds. That means that the Gaussian noise predominates when the sampling integration time is less than 7 seconds. When the sampling integration time exceeds 7 seconds, the Allen variance of the measured data rises slowly with the increase of the sampling time. That means that the flicker noise or random-walk noise predominates when the sampling integration time is greater than 7 seconds. So, the optimal averaging time is about 7 seconds from Fig. 5.

With the data received by all the antenna elements, the optimal averaging time of the SAIR system is measured by using the proposed method. The result of the system's optimal averaging time is plotted in Fig. 6. From Fig. 6, the system's optimal averaging time is about 5–10 second, and the mean value of the system's optimal averaging time is about 6.8 seconds.

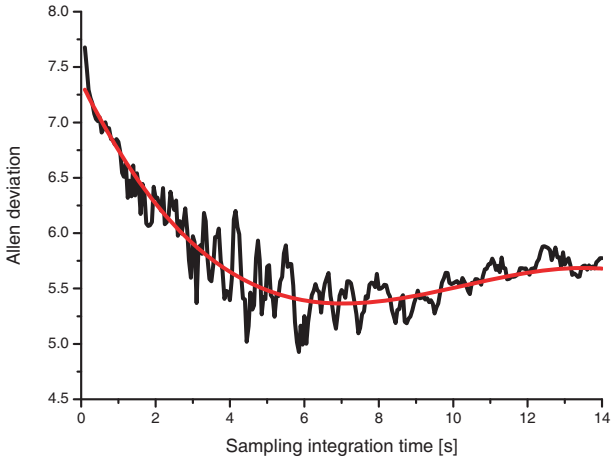

Figure 5. The Allen deviation of the data measured by two receivers.

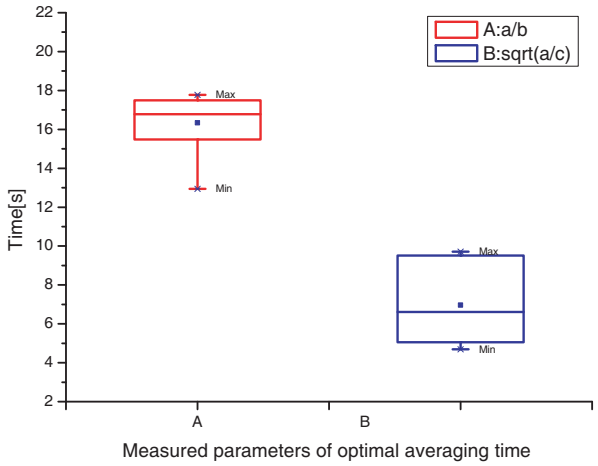

Figure 6. The measured optimal averaging time of SAIR testing system.

In addition, the optimal sampling averaging time of the system is mainly affected by the random-walk noise from Fig. 6. This is because that the receiving channel of the test system does not take any temperature control measures. From the result measured in Fig. 6, it provides guidance for the future system design to take the temperature control measures to reduce the influence of the random-walk noise component and extend the optimal sampling time of the test system.

In order to verify the correctness of the above analysis results, an imaging experiment has been carried out. The schematic diagram of the imaging scene is shown in Fig. 7. A metal plate is placed about 34 meters away from the testing SAIR system. The size of the metal plate is about 20 cm $\times$ 20 cm.

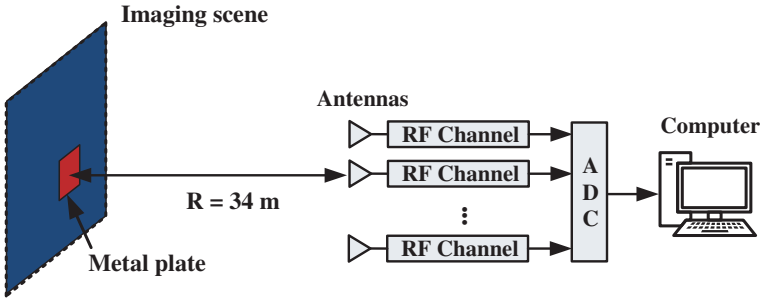

Figure 7. Schematic diagram of the experimental test scene.

With the measured data, the imaging results are reconstructed with different sampling averaging times. Fig. 8(a)–Fig. 8(d) show the images recovered with 5, 8, 11, 14 seconds, respectively. The metal target denoted with the dash line is well reconstructed with high SNR when the sampling averaging time is 5 or 8 seconds. However, the amplitude of the reconstructed target decreases with the increased sampling averaging time. This is because the random-walk noise predominates when the sampling averaging time is greater than 8 seconds according to the above analyzed results.

Figure 9 shows the SNRs of the inversion results under different sampling integral time conditions. From Fig. 9, the SNR of the image will be improved with the increase of the sampling averaging time when the sampling averaging time is less than 8 seconds. When the sampling accumulation time is greater than 8 seconds, the SNR of the image decreases with the increase of the sampling accumulation time. This is consistent with the analysis results shown in Fig. 6, which proves the effectiveness of the noise behavior model and the optimal averaging time picking method.

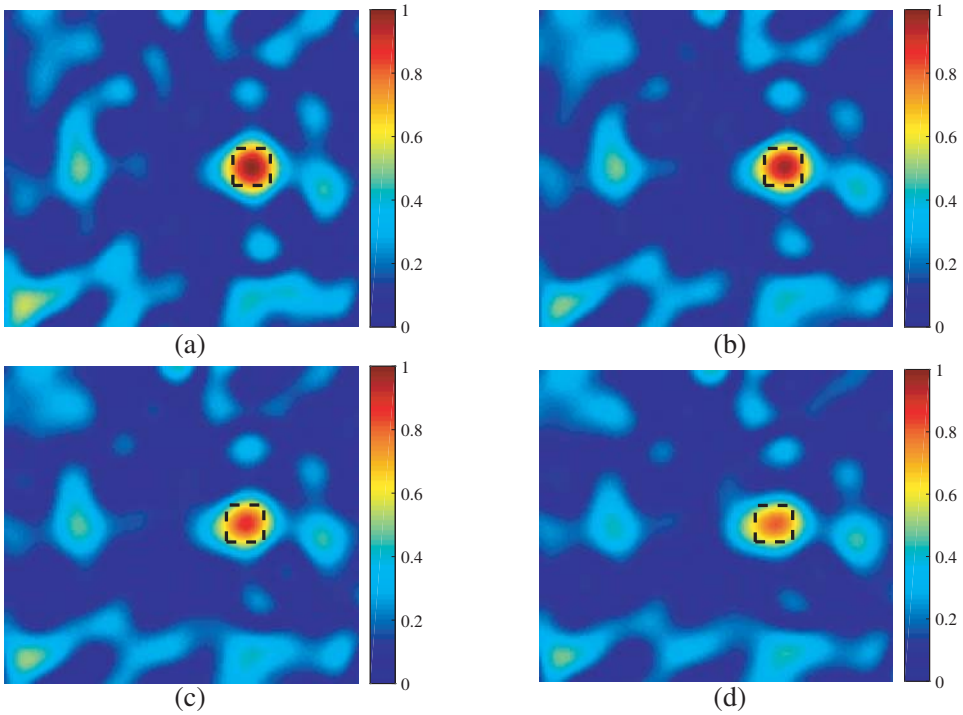

Figure 8. Images reconstructed with different sampling averaging time: (a) 5 seconds; (b) 8 seconds; (c) 11 seconds (d) 14 seconds.

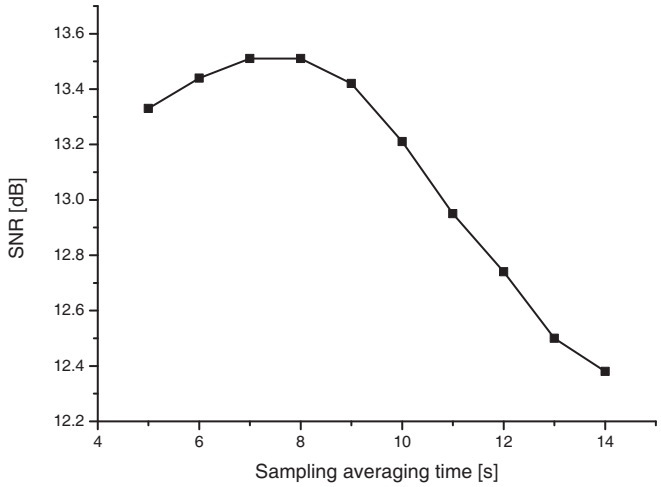

Figure 9. SNRs of images reconstructed with different sampling averaging time.

4. CONCLUSIONS

The main contribution of this paper is to model the noise behavior in the SAIR system and to present the method for picking the optimal averaging time for imaging in the SAIR system. With the SAIR testing system, some imaging experiments are carried out to validate the feasibility of the developed noise behavior model and the optimal averaging time picking method. With the noise behavior model and optimal averaging time picking method, it provides guidance for designing the SAIR system, correcting the system error and imaging with high fidelity.

ACKNOWLEDGMENT

This work was supported by the Science and Technology on Electronic Information Control Laboratory.

REFERENCES

1. Ulaby, F., R. Moore, and A. Fung, "Microwave remote sensing active and passive: Microwave remote sensing fundamentals and radiometry," *Addison Wesley Publishing Company*, 1–456, 1981.
2. Carmona, A. J., "Application of interferometric radiometry to earth observation," Univ. Politècnica Catalunya, Barcelona, Spain, 1997.
3. Mann, C., "A compact real time passive terahertz imager," *Proceedings of SPIE*, Vol. 6211, 1–5, 2006.
4. Luukanen, A., L. Gronberg, M. Gronholm, P. Lappalainen, M. Leivo, A. Rautiainen, A. Tamminen, J. Ala-Laurinaho, C. Dietlein, and E. Grossman, "Real-time passive terahertz imaging system for standoff concealed weapons imaging," *Proceedings of SPIE*, Vol. 7670, 1–8, 2010.
5. May, T., G. Zieger, S. Anders, V. Zakosarenko, M. Starkloff, H. G. Meyer, G. Thorwirth, and E. Kreysa, "Passive stand-off terahertz imaging with 1 hertz frame rate," *Proceedings of SPIE*, Vol. 6949, 1–8, 2008.
6. Su, K., Z. Liu, R. B. Barat, D. E. Gary, Z. Michalopoulou, and J. F. Federici, "Two dimensional interferometric and synthetic aperture imaging with a hybrid terahertz/millimeter wave system," *Applied Optics*, Vol. 49, No. 19, 13–19, 2010.
7. Corbella, I., F. Torres, A. Camps, A. Colliander, M. Martín-Neira, S. Ribó, K. Rautiainen, N. Duffo, and M. Vall-llossera, "MIRAS end-to-end calibration: Application to SMOS L1 processor," *IEEE Transactions on Geoscience and Remote Sensing*, Vol. 43, No. 5, 1126–1134, 2005.
8. McMullan, K. D., M. A. Brown, M. Martin-Neira, W. Rits, S. Ekholm, J. Matri, and J. Lemanczyk, "SMOS: The payload," *IEEE Transactions on Geoscience and Remote Sensing*, Vol. 46, No. 3, 594–605, 2008.
9. Gaier, T., P. Kangaslahti, B. Lambrigtsen, I. Ramos-Perez, A. Tanner, D. McKague, C. Ruf, M. Flynn, Z. Zhang, R. Backhus, and D. Austerberry, "A 180 GHz prototype for a geostationary microwave imager/sounder-GeoSTAR-III," *2016 IEEE International Geoscience and Remote Sensing Symposium*, 2021–2023, 2016.
10. Land, D. V., A. P. Levick, and J. W. Hand, "The use of the Allen deviation for the measurement of the noise and drift performance of microwave radiometers," *Measurement Science and Technology*, Vol. 18, No. 7, 1917–1928, 2007.
11. Chen, J., Y. Li, J. Wang, Y. Li, and Y. Zhang, "Regularization imaging algorithm with accurate G matrix for near-field MMW synthetic aperture imaging radiometer," *Progress In Electromagnetics Research B*, Vol. 58, 193–203, 2014.
12. Chen, J., Y. Li, J. Wang, Y. Li, and Y. Zhang, "An accurate imaging algorithm for millimeter wave synthetic aperture imaging radiometer in near-field," *Progress In Electromagnetics Research*, Vol. 141, 517–535, 2013.
13. Wells, J., W. Daywitt, and C. Miller, "Measurement of effective temperatures of microwave noise sources," *IEEE Transactions on Instrumentation Measurement*, Vol. 13, No. 1, 17–28, 1964.
14. Ziel, A., *Noise in Measurements*, Chapter 7, Wiley, New York, 1976.
15. Cowley, A. M. and H. O. Sorensen, "Quantitative comparison of solid-state microwave detectors," *IEEE Transactions on Microwave Theory and Techniques*, Vol. 14, No. 12, 588–602, 1967.
16. Barnes, J., A. Chi, L. Cutler, D. Healey, D. Leeson, T. McGunigal, Jr. Mullen, W. Smith, R. Sydnor, R. Vessot, and G. Winkler, "Characterization of frequency stability," *IEEE Transactions on Instrumentation Measurement*, Vol. 20, No. 2, 105–120, 1971.
17. Allan, D., "Should the classical variance be used as a basic measure in standards metrology?," *IEEE Transactions on Instrumentation Measurement*, Vol. 36, No. 2, 646–654, 1987.